PAPER • OPEN ACCESS

Anomalous Nernst effect in Co_2MnSi thin films

View the article online for updates and enhancements.

IOP ebooks™

Bringing you innovative digital publishing with leading voices to create your essential collection of books in STEM research.

Start exploring the collection - download the first chapter of every title for free.

Anomalous Nernst effect in Co₂MnSi thin films

C D W Cox[1], A J Caruana[2], M D Cropper[1] and K Morrison[1]

[1] Department of Physics, Loughborough University, Loughborough, Leicestershire, LE11 3TU, United Kingdom
[2] ISIS Neutron and Muon Source, Didcot, Oxfordshire, OX11 0QX, United Kingdom

E-mail: c.d.w.cox@lboro.ac.uk

CrossMark

Abstract

Separation of the anomalous Nernst and spin Seebeck voltages in bilayer devices is often problematic when both layers are metallic, and the anomalous Nernst effect (ANE) becomes non-negligible. Co_2MnSi, a strong candidate for the spin generator in spin Seebeck devices, is a predicted half-metal with 100% spin polarisation at the Fermi energy, however, typically B2 or $L2_1$ order is needed to achieve this. We demonstrate the optimisation of thin film growth of Co_2MnSi on glass, where choice of deposition and annealing temperature can promote various ordered states. The contribution from the ANE is then investigated to inform future measurements of the spin Seebeck. A maximum ANE coefficient of 0.662 μV K^{-1} is found for an A2 disordered polycrystalline Co_2MnSi film. This value is comparable to ordered Heusler thin films deposited onto single crystal substrates but obtained at a far lower fabrication temperature and material cost.

Keywords: Heusler alloy, anomalous Nernst effect, half-metal, thin films

(Some figures may appear in colour only in the online journal)

1. Introduction

Heusler alloys have provided a broad range of materials for research over the past 100 years, with respect to magnetic shape memory [1], magnetocaloric properties [2] and more recently applications in spintronic devices, which utilise the spin of the electrons (whether they be in insulators or metals) [3, 4]. In addition to these characteristics, recent density functional theory (DFT) calculations have shown that certain alloys exhibit a strong anomalous Hall conductivity and therefore, by extension, should also show a high anomalous Nernst response believed to be driven by the enhanced Berry curvature [5,6].

Primarily divided into two *taxa*, half Heuslers (*XYZ*), formed of elements with a 1:1:1 ratio, crystallise in a C1b structure [7], whereas the full Heuslers (*X₂YZ*) crystallise in the $L2_1$ structure. The latter group shall be the focus of

this work, more specifically the predicted half-metallic ferromagnet, Co_2MnSi (CMS). The density of states (DOS) of CMS predicts a bandgap of the minority spin state at the Fermi level [8], for the fully ordered alloy ($L2_1$), with non-zero density for the majority spin state at the Fermi energy, ε_F, which would result in 100% spin polarisation (SP). For this reason, there has been a steady increase in interest in the growth and development of CMS thin films for spintronics applications.

Examples of such applications include the use of Co_2MnSi as a spin injector in thin film thermoelectrics [9] or in current perpendicular-to-plane giant magnetoresistance junctions (CPP-GMR) [10–13] for magnetic random access memory (MRAM). The challenge, however, lies in the production of suitably ordered Co_2MnSi thin films, as the degree of atomic order within the film is expected to dramatically alter the DOS (and hence accessible spin polarization).

For Heuslers in particular, the introduction of disorder through the inclusion of anti-sites, site swapping or off-stoichiometric atomic ratios leads to a destruction of the bandgap and results in a loss of the predicted half-metallic nature of CMS [14]. Nonetheless, in recent years, it has been

J. Phys. D: Appl. Phys. **53** (2020) 035005

C D W Cox *et al*

reported that in a B2 ordered state (Mn and Si site swapping with respect to $L2_1$); the half metallic property can still be maintained [15]. Other disordered structures for the Co_2MnSi alloy include DO3 (Co and Mn site swapping with respect to $L2_1$) and A2 (Co, Mn and Si site swapping with respect to $L2_1$), both of which have been shown to destroy the half-metallicity [14].

There is, however, limited experimental evidence of 100% SP (whether bulk or surface), with only a handful of instances of this value being reported [16]. It is, therefore, crucial to investigate diligently the growth conditions which give rise to not only $L2_1$ ordered but also A2 or B2 disordered phases. The quality of such a Heusler film is typically investigated using x-ray diffraction (XRD) and reflectivity, magnetometry and resistivity measurements (all of which shall be covered in this work). Once the type of ordering in each film is confirmed, magnetothermal measurements can be used to probe the thermoelectric response, which for bare CMS films is a result of the anomalous Nernst effect (ANE) (as defined in figure 1).

In this work, we demonstrate that a vast range of growth and post-fabrication treatments can lead to Co_2MnSi thin films displaying order across the spectrum, from: A2 to B2 to $L2_1$. Previously, a wide range of substrates have been used to grow epitaxial, textured or randomly oriented polycrystalline Heusler thin films with varying degrees of success [17–24]. However, in this study, amorphous glass (SiO_2) has been chosen to investigate the potential for widespread use of CMS in thermoelectric generators, where it may be preferable to develop coatings on glass [25].

2. Methods

2.1. Fabrication

The Co_2MnSi thin film samples presented in this work were deposited on 0.5 mm thick 22×22 mm glass substrates (borosilicate cover slips, Agar Scientific). Prior to fabrication, the substrates were outgassed at 400 °C to pre-condition and remove impurities from the surfaces of the amorphous SiO_2 substrates. The Co_2MnSi films were then deposited using a pulsed Nd:YAG ($\lambda = 532$ nm) laser operating at a repetition rate of 10 Hz from a single stoichiometric Co_2MnSi (Pi-Kem, purity $= 99.9\%$) target with a laser fluence of 5.2 J cm^{-2}. All samples were deposited under UHV at a typical base pressure 2×10^{-10} mbar and a target to substrate distance of 110 mm.

2.2. Analysis

X-ray diffraction (XRD) patterns of the films were obtained using a Bruker D2 Phaser with incident wavelength (Cu Kα) $\lambda = 1.54$ Å and divergent slit width $= 1$ mm. The measurements were taken in θ/θ geometry with the diffracted beam optics composed of 0.5 mm Ni monochromator and 2.5$''$ Soller slit followed by a 1D LYNXEYE™ detector with the detector opening set at 5.85°. XRD peaks were fitted with a Pseudo-Voigt function to assess the crystallite size using the

Scherrer equation, with the bulk lattice parameter $a_1 = 5.654$ Å as a guideline [26].

Grazing incidence x-ray diffraction (GIXRD) and x-ray reflectivity (XRR) were obtained using a Siemens D5000, with incident wavelength Cu Kα, $\lambda = 1.54$ Å; the incident beam was defined by a slit of width 0.05 mm. The diffracted beam optics for GIXRD composed of 2.5° Cu long Soller slits with a LiF monochromator and a scintillation detector. The diffracted beam optics for XRR were as follows; 0.1 mm receiving slit, 0.6 mm anti-scatter slit, 0.2 mm detector slit, graphite monochromator and scintillation detector. XRR data were fitted using the opensource GenX program [27] and the resulting scattering length density (SLD) profile from the model was used to obtain the mass density, roughness and thickness of the films.

Van der Pauw measurements were taken using a Keithley 6221/2182A current source and nanovoltmeter in conjunction with a Keithley 705 switch system. Magnetic hysteresis loops were obtained using a vibrating sample magnetometer (Cryogenic Ltd). Magneto-thermoelectric measurements (ANE) were obtained using an in-house built system comprising: two Peltier cells, one acting as heat source and the other as a monitor; type E thermocouples to monitor the temperature difference between the top and bottom of the sample; and a nanovoltmeter to monitor voltages generated by the ANE and spin Seebeck effect. Calibration of the Peltier cells was carried out using a known heater in various geometries, similar to the method of Sola *et al* [28] with full details given in [29, 30].

3. Results

3.1. Deposition temperature (T_{Dep})

In this section, we present results on the optimization of the substrate (deposition) temperature (stabilized to ±1 °C) of the Co_2MnSi films where the nomenclature is CT followed by the deposition temperature (RT is room temperature). See table 1 for the composition and deposition conditions of each sample.

For structural analysis, out of plane XRD was obtained, as shown in figure 2(a). At low deposition temperatures ($T_{Dep} < 100$ °C), amorphous films were produced, indicated by the absence of any discernible Bragg reflections. These films (due to their amorphous nature) would be expected to have higher resistivity ($\rho > 100$ $\mu\Omega$cm) compared to single crystal bulk ($\rho \sim 21$ $\mu\Omega$cm) [31], as seen in figure 2(c). At 170 °C, [2 2 0] textured crystalline films formed with primarily A2 order dominating most of the film volume. This is indicated by the emergence of the (2 2 0) peak and absence of (1 1 1), (2 0 0), (2 2 2) in XRD or GIXRD. Up to 200 °C all films exhibited A2 order, with the addition of the (2 0 0) and (4 0 0) reflections at $T_{Dep} \geqslant 300$ °C that suggest the onset of B2-type order.

GIXRD was also used to investigate the structure, as shown in figure 2(b) where the progression from amorphous to crystalline films was observed as T_{Dep} increased from 100 °C to 170 °C. Upon increasing the deposition temperature up to

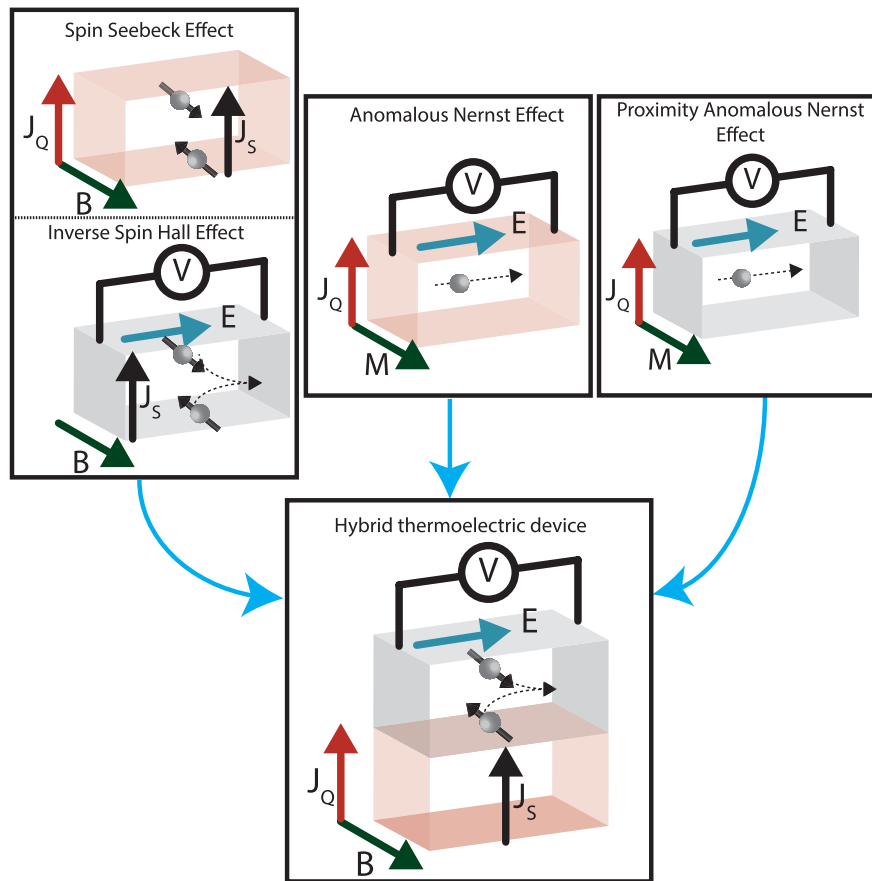J. Phys. D: Appl. Phys. **53** (2020) 035005

C D W Cox *et al*

Figure 1. Schematic of the spin Seebeck, inverse spin Hall, anomalous Nernst and proximity induced ANEs, all of which contribute to the observed voltage in a typical bilayer thin film thermoelectric hybrid device.

500 °C an increase in the long-range L2$_1$ order was observed as indicated by the presence of the (1 1 1) superlattice reflection. At substrate temperatures exceeding 500 °C, significant phase separation of Co and MnSi compounds occurred, as indicated by the emergence of the Co (1 1 1) reflection in GIXRD.

X-ray reflectivity (XRR) curves were taken for all samples, from which the film thickness (shown in table 1), density and roughness were determined. Figure 2(d) shows representative XRR curves and fits for CT170 and CT600. There is an obvious damping of the Keissig fringes as T_{Dep} was increased, indicating a significant increase in the mismatch between surface and interface roughness at higher temperatures. This conclusion agrees well with the SLD profiles (figure 2(d) inset) generated from the fit, where the interface width for CT600 was far greater than in CT170 with regards to magnetisation (not shown here), these films exhibited decreasing coercive fields as T$_{Dep}$ was increased, which is attributed to the onset of long-range ordering.

To summarise, polycrystalline Co$_2$MnSi thin films were prepared by depositing at 170 °C $< T_{Dep} <$ 600 °C. For optimum L2$_1$ order, a deposition temperature of 500 °C is necessary, however high deposition temperatures are not often compatible with many thin film device fabrication methods. As a result, an investigation into post-deposition annealing was undertaken to determine whether B2 or L2$_1$ order could be recovered at lower temperatures.

Table 1. Summary of the key parameters for the deposition temperature, T_{Dep}, series. Thickness was determined from XRR, order was determined from XRD and GIXRD.

Sample	T_{Dep} (°C)	Thickness, t (nm)	Order
CTRT	23	74 ± 2	A2
CT100	100	53 ± 2	A2
CT170	170	56 ± 2	A2
CT200	200	62 ± 2	A2
CT300	300	56 ± 2	B2
CT400	400	51 ± 2	B2
CT500	500	48 ± 2	L2$_1$
CT600	600	41 ± 2	L2$_1$

3.2. Annealing temperature (T_{Ann})

For the post-deposition annealing study the substrates were cooled from the outgassing temperature of 400 °C to the deposition temperature, T_{Dep} = 170 °C, which was chosen due to the onset of crystalline order seen in figure 3(a). The deposition time was varied in order to achieve a nominal thickness of $t >$ 90 nm across the series, the samples were subsequently annealed *in situ* for 1 h at a maximum pressure of 4×10^{-8} mbar and temperatures ranging from 100 °C to 600 °C, as summarised in table 2. The nomenclature here is CA followed by the annealing temperature.
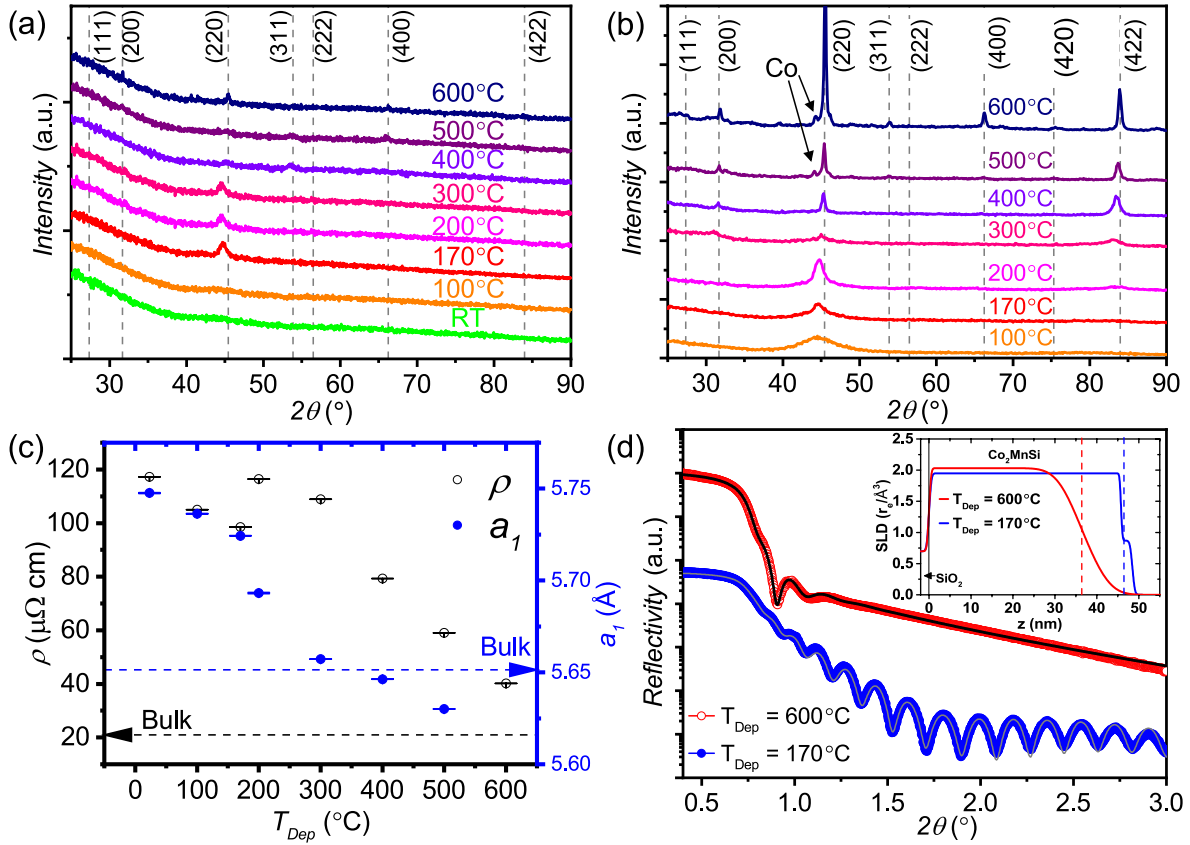
J. Phys. D: Appl. Phys. **53** (2020) 035005

C D W Cox *et al*

Figure 2. (a)–(d) Summary of the structural characterisation of the T_{Dep} series. (a) XRD, (b) GIXRD taken at $\omega = 0.8°$, (c) evolution of room temperature resistivity (open circles) and lattice parameter (closed circles) with T_{Dep} and (d) XRR (and fits) and corresponding SLD profiles for CT170 (closed circles and grey line) and CT600 (open circles and black line).

Figure 3 shows the evolution of A2, B2 and L2₁ order with T_{Ann}, as indicated by XRD and GIXRD. After annealing, the films all exhibited strong $(2\,2\,0)$ texture out of plane. Low intensity $(4\,4\,0)$ peaks were also observed for many of the films, substantiating the strong $(2\,2\,0)$ out of plane texture. At $T_{Ann} = 100$ °C and 200 °C A2 ordered films were produced stemming from the order seeded at $T_{Dep} = 170$ °C. Upon increasing the annealing temperature to 300 °C, B2 order was observed, as identified by the appearance of the $(2\,0\,0)$ reflection in GIXRD (figure 3(b)). Partial L2₁ ordering was achieved when annealed at 450 °C, where the $(1\,1\,1)$ reflection was present. At 600 °C, L2₁ order was maintained within the films, however with significant Co segregation identified by the Co $(1\,1\,1)$ reflection as a low angle shoulder of the CMS $(2\,2\,0)$ reflection [17].

The resistivity, ρ, and lattice parameter, a_1, are also shown in figure 3(c) where progression from highly strained resistive state (far from bulk value) towards an ordered state (close to bulk value) was seen as T_{Ann} was increased and the crystal structure moves from A2 to L2₁ order.

Vibrating sample magnetometry (VSM) was used to probe the magnetic characteristics of these annealed films. It can be seen from figure 3(d) that the coercive field increased as T_{Ann} increased from 100 °C to 200 °C. The coercive field then decreased from 200 °C, where a minimum value of $H_c = 14$ Oe was observed at 500 °C, which corresponds to highly ordered films seen in the literature [17, 32].

3.3. ANE in Co₂MnSi

For prospective thermoelectric devices that utilise the spin Seebeck effect and especially those involving ferromagnetic metals, the contribution from additional effects such as the anomalous Nernst (from the Co₂MnSi) or proximity induced anomalous Nernst (thermoelectric voltage arising from magnetised Pt) effects is significant [33–35]. As such, it is worth characterising the potential anomalous Nernst voltage that can be generated in CMS thin films measured under similar geometries. We, therefore, measured the magneto-thermoelectric voltage generated by the T_{Ann} series of CMS films in the longitudinal geometry (see figure 1) (where the magnetic field was in plane and perpendicular to the temperature gradient, which was out of plane). The ANE voltage can then be normalised to the temperature difference (ΔT), contact separation (L_y) and length over which the temperature difference is established (L_z),

$$S_{\Delta T} = \frac{V L_z}{\Delta T L_y}. \tag{1}$$

To compare to spin Seebeck measurements we measured the ANE as a function of both temperature difference, ΔT, and heat-flux, J_Q ($=Q/A$) where Q is the heat in W and A is the area of the sample in m². For the heat-flux measurement, the ANE can be calculated by,
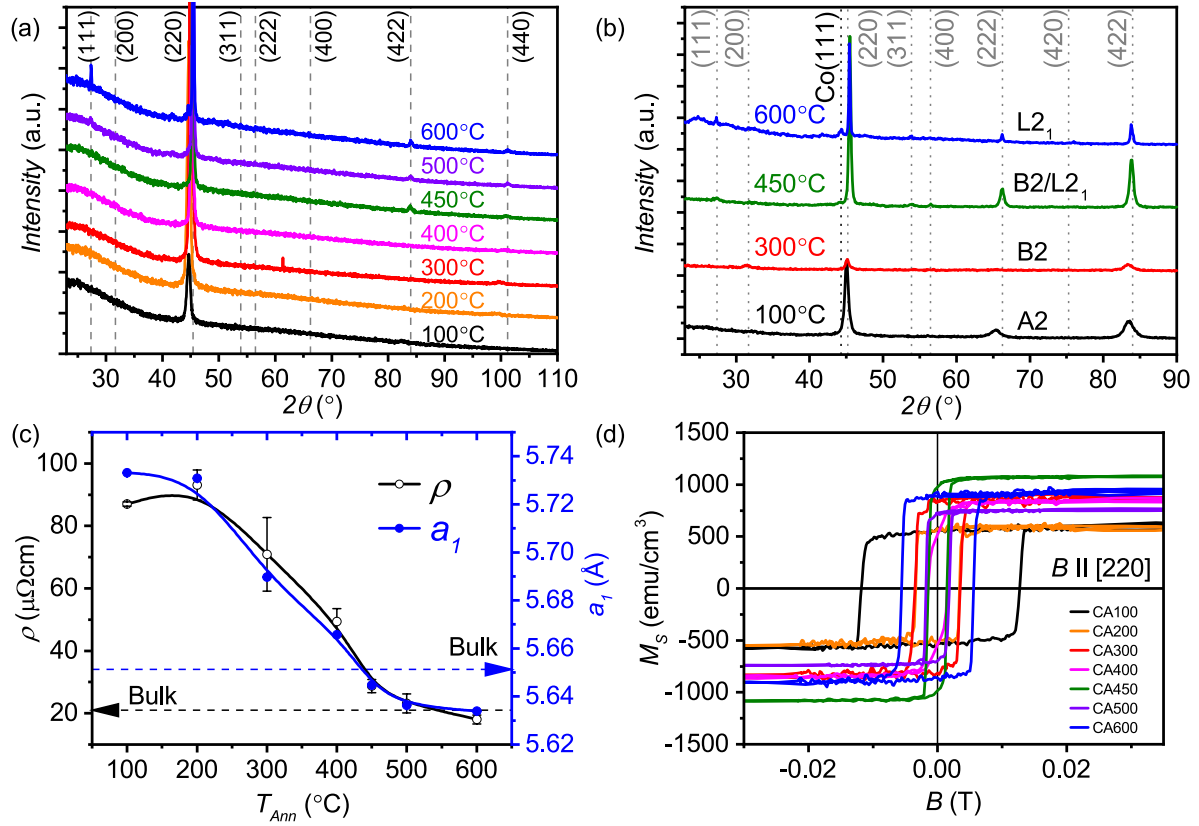
$$S_{J_Q} = \frac{V}{J_Q L_y}. \tag{2}$$

Figure 3. (a)–(d) Summary of the structural and magnetic characterisation of T_{Ann} series. (a) XRD patterns, (b) GIXRD patterns taken at $\omega = 0.7°$, (c) evolution of resistivity (open circles) and lattice parameter (closed circles) with T_{Ann} and (d) magnetization as a function of applied magnetic field (VSM).

Table 2. Summary of the key parameters for the annealing temperature, T_{Ann}, series.

Sample	T_{Ann} (°C)	Thickness, t (nm)	Order
CA100	100	99 ± 2	A2
CA200	200	122 ± 2	A2
CA300	300	92 ± 2	B2
CA400	400	106 ± 2	B2
CA450	450	122 ± 2	$L2_1$
CA500	500	111 ± 2	$L2_1$
CA600	600	111 ± 2	$L2_1$

The advantage of measuring the ANE with respect to J_Q is that it is insensitive to thermal interface offsets (due to losses at voltage contacts and interfaces) and the contribution of the substrate to the temperature gradient that plague thin film measurements [28]. Therefore, to subtract this substrate contribution, one uses the heat-flux method. In the steady state limit, the heatflow across layers connected in series is equal,

$$J_Q = \frac{\Delta T}{\left(L_1 / \kappa_1 \right) + \left(L_2 / \kappa_2 \right)} \tag{3}$$

where $L_{1,2}$ and $\kappa_{1,2}$ are the thicknesses and thermal conductivities of layers 1 and 2, respectively, and ΔT is the combined temperature difference. For a single layer this becomes:

$$J_Q = \frac{\Delta T_{Layer}}{\left(L_1 / \kappa_1 \right)}, \tag{4}$$

where ΔT_{Layer} is the temperature difference across layer 1. Substituting equation (4) into (2)

$$S_{JQ} = \frac{V}{\frac{\Delta T_{Layer} \, \kappa_1}{L_z} L_y}, \tag{5}$$

rearranging equation (5) gives

$$S_{JQ}\kappa_1 = \frac{V \, L_z}{\Delta T_{Layer} \, L_y} = \frac{V_{ANE}}{\Delta T_{Layer}} = S_{\Delta T}. \tag{6}$$

Therefore, to scale S_{JQ} to $S_{\Delta T}$ one needs only to multiply by the thermal conductivity, κ, of the active layer.

Alternatively, one can determine the temperature difference across the thickness of the active layer using;

$$\frac{J_Q \, L_1}{\kappa_1} = \Delta T_{Layer}. \tag{7}$$

This can then be used in equation (1) with corresponding film thickness L_z to calculate $S_{\Delta T}$. For the calculation of ΔT_{Layer} in this work, the thermal conductivity of Co_2MnSi was taken from Bosu et al [9] to be $\kappa = 11$ W/m/K.

Examples of the raw voltage versus heat-flux for sample CA200 are given in figure 4(a) alongside a confirmation of the linearity of $J_Q/\Delta T$ in figure 4(b). There is a clear magnetic hysteresis observed in the ANE voltage that can be attributed to the ANE and not background Seebeck voltages. As expected, the magnitude of the ANE voltage increases linearly with ΔT (figure 4(c)). Figure 4(d) shows the plot of VL_z/L_y versus ΔT_{Layer}, where the slope of the line gives $S_{\Delta T} = 0.662$ μV K^{-1} for CA200.

J. Phys. D: Appl. Phys. **53** (2020) 035005
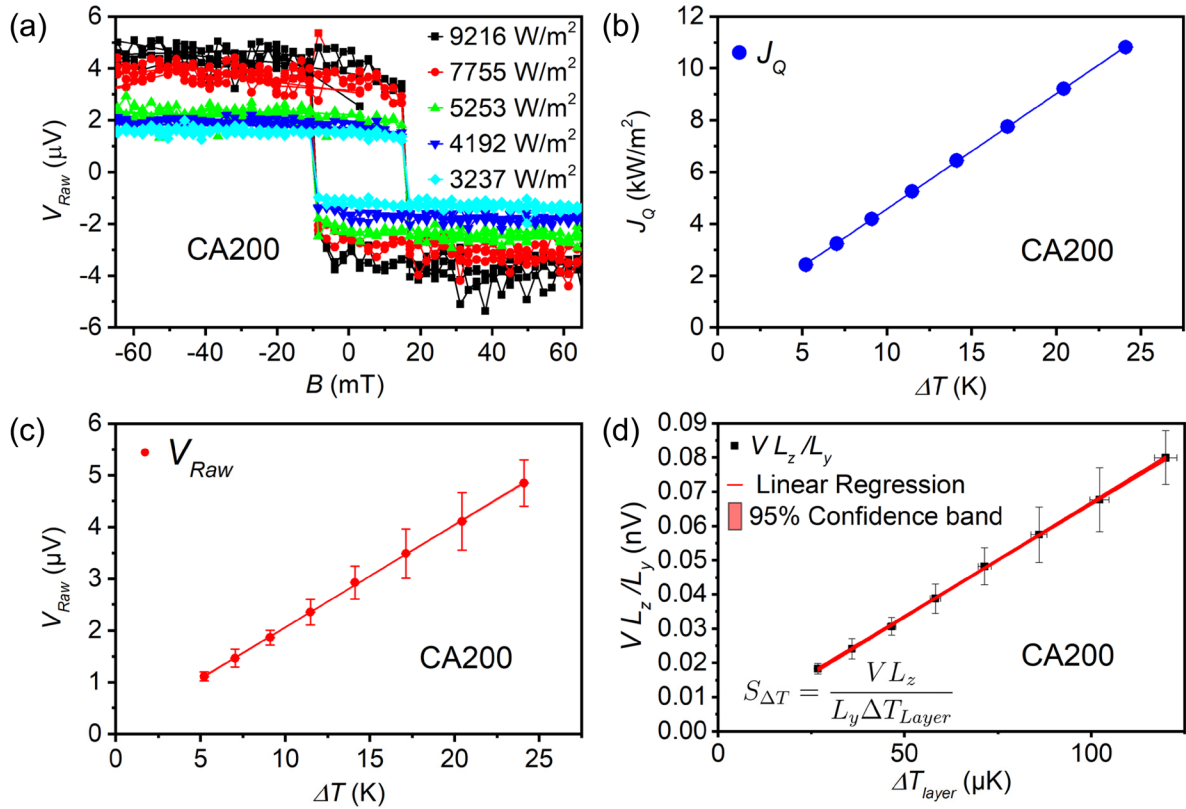
C D W Cox *et al*

Figure 4. Example ANE results of CA200 sample (a) Raw voltage (V_{Raw}) as a function of magnetic field B for different heat-flux (J_Q) and (b) J_Q (closed symbols) versus ΔT, the error bars are smaller than the size of the symbols. (c) Linear fit of V_{Raw} versus ΔT and (d) V_{ANE} versus ΔT_{Layer}, where the slope of the linear fit is the value of the $S_{\Delta T}$ coefficient given by equation (6), the 95% confidence band is displayed as a guide for the eye.

Figure 5 shows a summary of the $S_{\Delta T}$ values of the remaining T_{Ann} series. Interestingly, the magnitude of the signal decreased for increasing order i.e. from A2-B2-L2$_1$. For the B2 ordered CA300 film, the ANE fell to 0.461 μV K^{-1}, 70% of the CA200 film. The L2$_1$ ordered CA500 film had a significantly reduced ANE signal compared to both films of 0.114 μV K^{-1}. This can be explained by the onset of phase segregation which ultimately leads to a reduced fraction of Co$_2$MnSi. For CA600 no ANE signal was detectable above the noise limits of the measurement.

The saturation magnetisation (M_{Sat}) of the films has been plotted alongside the ANE data. It is clear that the A2 films exhibited a lower M_{Sat} than the B2 and L2$_1$ films, whilst their ANE signal was higher. The increase in M_{Sat} for CA600 is due to Co segregation and the influence of Co domains.

4. Discussion

Highly $(2\,2\,0)$ oriented A2 ordered Co$_2$MnSi films were grown on amorphous glass substrates at 170 °C with B2 order dominating between 300 °C and 500 °C and L2$_1$ order emerging at 600 °C. For growth temperatures higher than 400 °C, however, phase segregation occurred in line with previous research [12]. Post-deposition annealing was investigated at temperatures up to 600 °C, on films deposited at 170 °C. At $T_{Ann} = 300$ °C, B2 order was found and L2$_1$ order

was achieved at the lower temperature of 450 °C instead of a deposition temperature of 600 °C, owing to the initial crystallisation at 170 °C. Further increasing the annealing temperature to 600 °C, led to phase segregation as seen in the T_{Dep} study.

Studying the anomalous Nernst properties of the T_{Ann} series, the optimal ANE signal of 0.6623 μV K^{-1} was obtained for $T_{Ann} = 200$ °C. This value is larger than the ternary Heusler Co$_2$TiSn, CTS, (0.15 μV K^{-1}) but not as large as the quaternary Co$_2$Ti$_{0.6}$V$_{0.4}$Sn, CTVS, (1.8 μV K^{-1}), where doping of the CTS lattice with V leads to a shift of the Fermi-level which induces an enhanced anomalous Hall Effect (AHE) [36].

An interesting point to note is that ordinarily the ANE is assumed to be related to the magnetisation of the film, however, from figure 5, the trend of the magnetisation (which peaks at CA450) does not follow that of the ANE (peaks at CA200) suggesting a secondary contribution other than magnetisation. Firstly, we consider that our measurement assumes a constant thermal conductivity $\kappa = 11$Wm^{-1} K^{-1} across all samples. Based on the Wiedemann-Franz law, $\kappa = LT/\rho$, where L is the Lorenz number, T is the temperature and ρ is the resistivity, we can normalise our ANE coefficient, $S_{\Delta T}$, by ρ to factor in any changes in κ across the T_{Ann} series. Given the similar trend seen in the resistivity in figure 3 and the ANE in figure 5, our assumption of a constant κ across the series holds and so the secondary contribution must arise from another source.
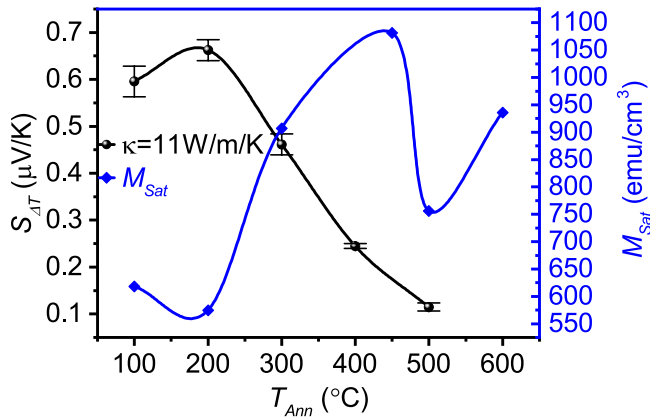
Figure 5. Summary of the $S_{\Delta T}$ versus magnetization for the T_{Ann} series. Calculation of $S_{\Delta T}$ assuming a thermal conductivity, κ, of 11 $Wm^{-1}K^{-1}$.

In recent studies, this contribution is thought to originate from the band structure of the material, upon which, order and doping have been suggested as a mechanism for manipulation of nodal lines, thought to be one contribution to the enhanced AHE (and therefore ANE) [37]. In this study, whilst the band structure of $L2_1$ ordered CMS may not display these exotic phenomena, the influence of disorder and possible off-stoichiometry may explain the enhanced ANE in A2 disordered films over $L2_1$ ordered films.

Other materials investigated for the ANE include chiral antiferromagnet, Mn_3Sn alloys [38], and perpendicularly magnetised FePt [39], FePd, MnGa alloys and Co/Ni bilayers [40]. Of these, FePt is the only material to exhibit a larger ANE than the Co_2MnSi reported here.

This being said, the magnitude of the ANE in Co_2MnSi is an order of magnitude lower than that which is found in Co_2MnGa (CMG) where the ANE was observed to be approximately 6 $\mu V\ K^{-1}$ for single crystals [6] and 2 $\mu V\ K^{-1}$ [41] for thin films. This significantly larger signal is believed to originate from the enhanced Berry curvature around the Fermi energy, ε_F. Nevertheless, given the differences in experimental design (in-plane ΔT for CMG, CTS and CTVS and out-of-plane for CMS) the values obtained here are in agreement with previous values of the Co-based full Heuslers.

Due to the tunability of the Heusler alloys through doping and stoichiometry engineering, several materials [42, 43] are now being investigated with the motivation being to tune the DOS, enhancing the anomalous Hall effect which in turn is believed to produce a significantly increased ANE voltage.

5. Conclusion

To summarise, we have experimentally investigated the impact of deposition temperature and annealing temperature on the crystal structure and magneto-thermoelectric effects in Co_2MnSi thin films on glass. We found that a minimum T_{Dep} of 170 °C was necessary to seed crystalline order in the films, with control over the development of A2, B2 or $L2_1$ order through the choice of higher T_{Dep} or T_{Ann}. The corresponding ANE voltage peaked for $T_{Ann} = 200$ °C where A2 atomic order is observed which is contrary to the model for

ANE and suggesting that the effort to fabricate perfect $L2_1$ ordering is not needed for the ANE.

Overall, we have demonstrated that ordered thin films of Co_2MnSi on glass produce an equivalent or larger signal than the majority of materials grown on single crystal substrates, opening up the field of polycrystalline thin films for thermoelectrics.

ORCID iDs

C D W Cox ⬤ https://orcid.org/0000-0003-2889-9751
M D Cropper ⬤ https://orcid.org/0000-0002-6104-8062
K Morrison ⬤ https://orcid.org/0000-0001-5672-3310

References

[1] Ullakko K, Huang J K, Kantner C, O'Handley R C and Kokorin V V 1996 *Appl. Phys. Lett.* **69** 1966–8
[2] Planes A, Mañosa L and Acet M 2009 *J. Phys.: Condens. Matter* **21** 233201
[3] Fetzer R *et al* 2015 *Sci. Rep.* **5** 8537
[4] Nedelkoski Z, Hasnip P J, Sanchez A M, Kuerbanjiang B, Higgins E, Oogane M, Hirohata A, Bell G R and Lazarov V K 2015 *Appl. Phys. Lett.* **107** 212404
[5] Miyasato T, Abe N, Fujii T, Asamitsu A, Onoda S, Onose Y, Nagaosa N and Tokura Y 2007 *Phys. Rev. Lett.* **99** 086602
[6] Guin S N *et al* 2019 *NPG Asia Mater.* **11** 16
[7] Graf T, Felser C and Parkin S S P 2011 *Prog. Solid State Chem.* **39** 1–50
[8] Comtesse D, Geisler B, Entel P, Kratzer P and Szunyogh L 2014 *Phys. Rev.* B **89** 094410
[9] Bosu S, Sakuraba Y, Uchida K, Saito K, Ota T, Saitoh E and Takanashi K 2011 *Phys. Rev.* B **83** 224401
[10] Yakushiji K, Saito K, Mitani S, Takanashi K, Takahashi Y K and Hono K 2006 *Appl. Phys. Lett.* **88** 98–101
[11] Iwase T, Sakuraba Y, Bosu S, Saito K, Mitani S and Takanashi K 2009 *Appl. Phys. Express* **2** 063003
[12] Sakuraba Y, Iwase T, Saito K, Mitani S and Takanashi K 2009 *Appl. Phys. Lett.* **94** 012511
[13] Kodama K, Furubayashi T, Sukegawa H, Nakatani T M, Inomata K and Hono K 2009 *J. Appl. Phys.* **105** 07E905
[14] Picozzi S, Continenza A and Freeman A J 2004 *Phys. Rev.* B **69** 094423
[15] Özdoğan K and Galanakis I 2011 *J. Appl. Phys.* **110** 076101
[16] Jourdan M *et al* 2014 *Nat. Commun.* **5** 3974
[17] Hirohata A, Ladak S, Aley N P and Hix G B 2009 *Appl. Phys. Lett.* **95** 252506
[18] Sakuraba Y, Nakata J, Oogane M, Kubota H, Ando Y, Sakuma A and Miyazaki T 2005 *Japan. J. Appl. Phys.* **44** L1100–2
[19] Kämmerer S, Heitmann S, Meyners D, Sudfeld D, Thomas A, Hütten A and Reiss G 2003 *J. Appl. Phys.* **93** 7945–7
[20] Pandey H, Joshi P C and Budhani R C 2013 *AIP Conf. Proc.* **1512** 1110–1

J. Phys. D: Appl. Phys. 53 (2020) 035005

C D W Cox *et al*

[21] Bosu S, Sakuraba Y, Saito K, Wang H, Mitani S and Takanashi K 2010 *Phys. Rev.* B **81** 054426

[22] Nakatani T M, Takahashi Y K, Ishikawa T, Yamamoto M and Hono K 2010 *J. Magn. Magn. Mater.* **322** 357–61

[23] Wolf G, Hamrle J, Trudel S, Kubota T, Ando Y and Hillebrands B 2011 *J. Appl. Phys.* **110** 043904

[24] Kawano M, Yamada S, Oki S, Tanikawa K, Miyao M and Hamaya K 2013 *Japan. J. Appl. Phys.* **52** 04CM06

[25] Kirihara A *et al* 2016 *Sci. Rep.* **6** 23114

[26] Webster P J 1971 *J. Phys. Chem. Solids* **32** 1221–31

[27] Björck M and Andersson G 2007 *J. Appl. Crystallogr.* **40** 1174–8

[28] Sola A, Bougiatioti P, Kuepferling M, Meier D, Reiss G, Pasquale M, Kuschel T and Basso V 2017 *Sci. Rep.* **7** 46752

[29] Morrison K, Caruana A J and Cox C 2017 (arXiv:1705.02491)

[30] Venkat G, Rose T A, Cox C D W, Stenning G B G, Caruana A J and Morrison K 2019 *Europhys. Lett.* **126** 37001

[31] Ritchie L, Xiao G, Ji Y, Chen T Y, Chien C L, Zhang M, Chen J, Liu Z, Wu G and Zhang X X 2003 *Phys. Rev.* B **68** 104430

[32] Singh L J, Barber Z H, Miyoshi Y, Branford W R and Cohen L F 2004 *J. Appl. Phys.* **95** 7231–3

[33] Nakayama H *et al* 2013 *Phys. Rev. Lett.* **110** 206601

[34] Kuschel T *et al* 2015 *Phys. Rev. Lett.* **115** 097401

[35] Klewe C, Kuschel T, Schmalhorst J-M, Bertram F, Kuschel O, Wollschläger J, Strempfer J, Meinert M and Reiss G 2016 *Phys. Rev.* B **93** 214440

[36] Hu J *et al* 2018 *Phys. Rev. Appl.* **10** 044037

[37] Ernst B *et al* 2019 *Phys. Rev.* B **100** 054445

[38] Ikhlas M, Tomita T, Koretsune T, Suzuki M T, Nishio-Hamane D, Arita R, Otani Y and Nakatsuji S 2017 *Nat. Phys.* **13** 1085–90

[39] Mizuguchi M, Ohata S, Uchida K, Saitoh E and Takanashi K 2012 *Appl. Phys. Express* **5** 093002

[40] Hasegawa K, Mizuguchi M, Sakuraba Y, Kamada T, Kojima T, Kubota T, Mizukami S, Miyazaki T and Takanashi K 2015 *Appl. Phys. Lett.* **106** 051103

[41] Reichlova H *et al* 2018 *Appl. Phys. Lett.* **113** 212405

[42] Guin S N *et al* 2019 *Adv. Mater.* **1806622** 1806622

[43] Noky J, Xu Q, Felser C and Sun Y 2019 *Phys. Rev.* B **99** 165117